Smectic Layer Origami via Preprogrammed Photoalignment

Ling-Ling Ma, Ming-Jie Tang, Wei Hu, Ze-Qun Cui, Shi-Jun Ge, Peng Chen,
Lu-Jian Chen, Hao Qian, Li-Feng Chi,* and Yan-Qing Lu**

Hierarchical architecture is of vital importance in soft materials. Focal conic domains (FCDs) of smectic liquid crystals, characterized by an ordered lamellar structure, attract intensive attention. Simultaneously tailoring the geometry and clustering characteristics of FCDs remains a challenge. Here, the 3D smectic layer origami via a 2D preprogrammed photoalignment film is accomplished. Full control of hierarchical superstructures is demonstrated, including the domain size, shape, and orientation, and the lattice symmetry of fragmented toric FCDs. The unique symmetry breaking of resultant superstructures combined with the optical anisotropy of the liquid crystals induces an intriguing polarization-dependent diffraction. This work broadens the scientific understanding of self-assembled soft materials and may inspire new opportunities for advanced functional materials and devices.

Mesoscopic hierarchical superstructures bridge the micro- and macroworlds, and play vital roles in materials science[1] and nanotechnology.[2] The beauty of nature, such as the iridescence in butterfly wings and peacock feathers,[3] the self-cleaning ability of lotus leaves,[4] and the water-repellent legs of water striders,[5] mostly comes from the exquisite ordered organizations with multiscale structures. It provides inspirations for the development of new functional materials via manipulating

the hierarchical architecture of various building blocks. Among them, liquid crystals (LCs) have attracted particular attention due to their excellent controllability of self-assembly behavior and the resultant physical properties.[6] Quintessential examples are the cholesteric LC featured by a spiral-twisted helical structure[7] and the blue-phase LC with a cylindrical double-twisted configuration,[8] which provide powerful tools for beam-steering,[7b,c] lasing,[9] displays,[10] etc. Recently, the focal conic domains (FCDs) of smectic LC (SLC) have been studied intensively because of their intriguing topological structures.[11] The hierarchical architecture of SLCs within the FCD lattice originates from two distinct levels. One is the unique parallel layer configuration inside a single FCD, where parallel layers are wrapped around a pair of conjugated defect lines of an ellipse and a one-branch hyperbola in orthogonal planes. The other is the 2D lattice of the periodic arrays formed of the basic units (i.e., the FCDs). Such deformed lamellar superstructures can lead to a variety of remarkable applications, including superhydrophobic surfaces,[12] microlens arrays,[13] soft lithographic templates,[14] and optical selective photomasks.[15] For all these applications, it is a fundamental and key requirement to precisely and freely control the hierarchical architecture of SLCs.

So far, much effort has been devoted to manipulating the FCD configurations. By tuning the film thickness[16] and sintering the SLC sample,[17] the domain size and smectic curvature can be altered, respectively. For a given SLC film thickness, the generated FCDs can also be adjusted via changing the external anchoring conditions. For example, the lattice symmetry of FCDs was manipulated by a multidirectional rubbing technique.[18] And substrates with alternating planar and homeotropic anchoring conditions were utilized to chemically confine FCDs individually, thus enabling the control of both size and arrangement of FCDs.[19] By further introducing artificial topographical substrates to increase the surface interactions with SLCs, the controllability of the spatial layer deformation can be significantly enhanced. Via presetting microchannels[20] or micropillars,[21] the domain size and lattice symmetry have been precisely controlled. Nevertheless, fabricating such chemical or geometrical patterns is usually complicated and time consuming; additionally, most reported results are limited to toric FCDs (TFCDs) with perfect rotational symmetry. If one could realize desired fragmented TFCDs which break the rotational symmetry while maintaining the radially gradient director field, two new dimensions besides the domain

L.-L. Ma, M.-J. Tang, Prof. W. Hu, S.-J. Ge, P. Chen,
Prof. Y.-Q. Lu
National Laboratory of Solid State Microstructures
Collaborative Innovation Center of Advanced
Microstructures and College of
Engineering and Applied Sciences
Nanjing University
Nanjing 210093, China
E-mail: huwei@nju.edu.cn; yqlu@nju.edu.cn
Dr. Z.-Q. Cui, Prof. L.-F. Chi
Jiangsu Key Laboratory for Carbon-Based Functional Materials
Institute of Functional Nano & Soft Materials (FUNSOM)
Soochow University
Suzhou 215123, China
E-mail: chilf@suda.edu.cn
Prof. L.-J. Chen
Department of Electronic Engineering
School of Information Science and Engineering
Xiamen University
Xiamen 361005, China
H. Qian
State Key Laboratory of Materials Oriented Chemical Engineering
College of Materials Science and Engineering
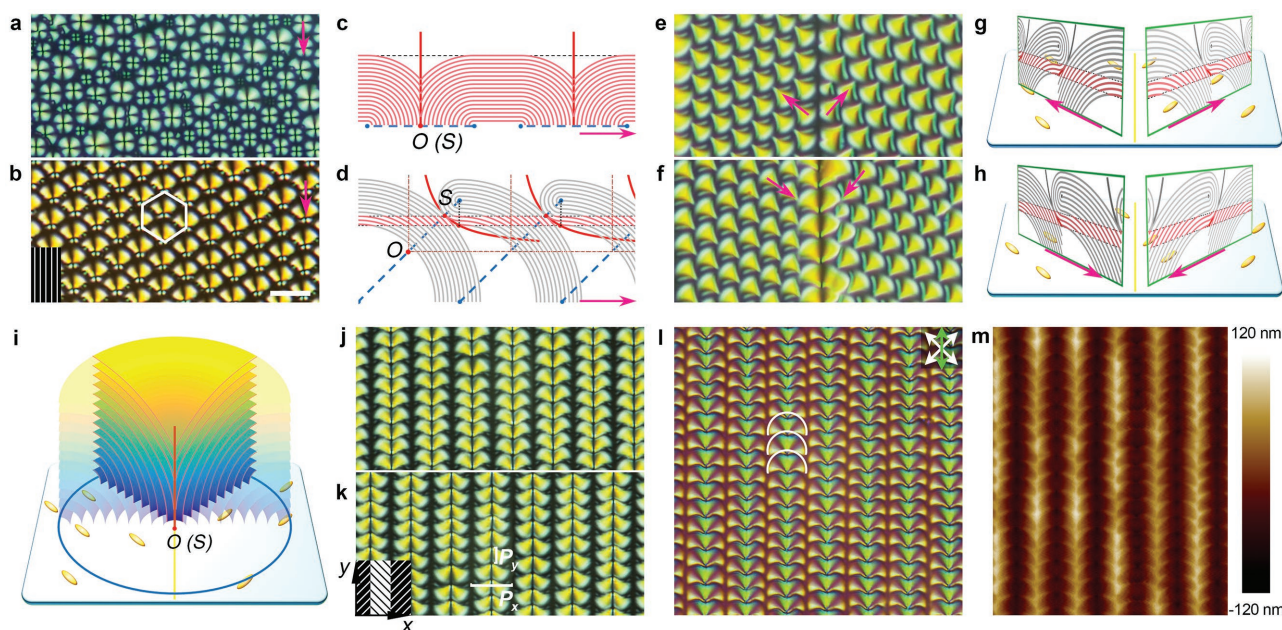Nanjing Tech University
Nanjing 210009, China

Figure 1. Focal conic domain lattices and corresponding layer configurations. POM textures of a) TFCDs on a random planar photoaligning surface and b) SFCDs on a unidirectional planar photoaligning surface, where the anchoring direction is indicated in the lower left corner. Corresponding vertical layer sections of c) TFCDs and d) SFCDs in the directions indicated by the pink arrows in (a) and (b). The range of existence of real SFCDs is highlighted in red.[22c] O and S indicate the geometric center of the ellipse and the singularity point, respectively. POM textures of SFCDs with e) a dark homeotropic wall and f) a series of semicircular FCDs on the alignment boundaries. g,h) Vertical layer sections of SFCDs along the anchoring directions of ±45° indicated by the pink arrows in (e) and (f). The golden bars represent the photoalignment agent. i) 3D model of the hemitoric focal conic structure. j–l) POM textures of hemitoric FCD superstructures under the same anchoring conditions indicated in (k). A sensitive tint plate was used to acquire the image presented in (l). The white semicircles illustrate the profiles of the hemitoric FCDs. The white and green arrows indicate the optical axes of the crossed polarizers and the tint plate, respectively, and the pair of polarizers was rotated by 45° with respect to the orientation used for the other texture observations. m) AFM image corresponding to (j). The scale bar represents 10 µm for all of the POM textures and the AFM image.

size and lattice symmetry: shape and orientation, could be introduced to the manipulation of hierarchical superstructures. This will drastically enrich the FCD family and extend their applications. Although there are a few noncircular FCDs generated via introducing predetermined geometry or molecular orientation,[22] it is still a great challenge to freely and simultaneously tailor the FCD configurations in hierarchical levels. Therefore, systematic work toward full control of the four dimensions (the domain size, shape, orientation, and the lattice symmetry) of FCDs is in high demand.

In the case that 3D nanometer-thin smectic layers could be controlled by a 2D preset surface, a practical approach for the realization of more fantastic hierarchical superstructures would be provided. A photoaligning technique is such a tool that can greatly facilitate the accurate anchoring direction control and arbitrary alignment pattern generation in LCs. It avoids most drawbacks caused by the traditional rubbing such as contamination, mechanical damage, and electrostatic charge.[23] Here, we demonstrate the smectic layer origami (a Japanese art of constructing 3D objects via bending or folding of pieces of paper) with a preprogrammed photoaligning surface. By this means, various distinct fragmented TFCDs are generated and both the geometry and the clustering characteristic of FCDs are freely tailored. Due to the rotational symmetry breaking of the FCD units, the emerging periodic fragmented TFCDs exhibit a metasurface-like polarization-dependent diffraction phenomenon. This work may extend the fundamental understanding

of self-assembled soft materials and enhance the construction of remarkable hierarchical superstructures. It may also open up new opportunities in advanced functional materials and novel photonic applications.

It is known that the equilibrium configuration of FCDs is determined by the smectic layer elasticity and the surface energy anisotropy.[20c] When an SLC 8CB is spin-coated onto a random planar photoaligning surface, circular-based TFCDs with zero eccentricities appear without size uniformity and positional ordering (**Figure 1**a). The defect pairs of TFCDs are degenerated into straight lines vertically passing through the centers of the circles[24] as shown in Figure 1c and Figure S1a,b (Supporting Information). If a substrate is treated with a unidirectional planar photoalignment, square FCDs (SFCDs) with a uniform domain size and a high eccentricity of $e = 1/\sqrt{2}$ are induced, self-assembling into a hexagonal lattice (Figure 1b). As shown in Figure 1d and Figure S1c,d (Supporting Information), the square focal conic structure has a pair of perpendicular asymptotes of the hyperbola defect line, with one of them being vertical to the substrate, hence the name of SFCD.[22c]

For a planar photoaligning surface with the anchoring directions being ±45° with respect to the alignment boundary, a two-domain array of SFCDs with orthogonal eccentric directions parallel to the underlying anchoring is generated. Because of the near-zero pretilt angle of the SLCs induced by the photoalignment agent[25] combined with the head-tail equivalence of the LC directors, SFCDs with opposite eccentric directions

occur with an equal probability. They can even coexist under the unidirectional anchoring condition (Figure S2, Supporting Information). Therefore, four possible cases of two-domain arrays are expected (Figure S3, Supporting Information). Because of the minimum free-energy requirement, however, only the mirror-symmetric cases are experimentally observed in Figure 1e,f. With the upper asymptotes normal to the substrate, corresponding vertical layer sections of the SFCDs are extracted along the anchoring directions (Figure 1g,h). Figure 1g indicates that the smectic layers tend to flatten over the alignment boundary, consistent with the observation of a dark homeotropic wall under a polarizing microscope (Figure 1e). By contrast, the two-sided SFCDs can also point to the alignment boundary, on which the singularity points (S) preferably nucleate (Figure 1h). Considering the layer continuity and the ±45° anchoring directions, local SLCs astride the boundary are in favor of sharing the same singularity point, resulting in a hemitoric FCD with the hyperbola degenerating toward a straight vertical line (Figure 1i). This means the eccentricity of the ellipse, e, approaches zero. As can be ascertained from the observed Maltese cross patterns, the singularity points are precisely located on the alignment boundary, which enables the manipulation of the FCD lattice. Compared to the TFCDs presented in most literatures,[26] such a fragmented toric focal conic structure exhibits a rotational symmetry breaking property but maintains a radially gradient director field. It is bound to add new features to the FCD family and enrich the applications of these highly ordered structures of defects.

To verify the manipulation of the hemitoric focal conic superstructures, periodically alternating ±45° alignment regions were produced. The alignment period $P_a = 10$ μm was chosen in accordance with the average diameter D_a (= 10.5 ± 0.2 μm) of the hemitoric FCDs in Figure 1f. Consequently, two types of ideal hemitoric focal conic superstructures with opposite domain orientations and a half-period shift were obtained over the entire substrate (Figure 1j,k). This phenomenon stems from two facts. First, the bottom anchoring cannot be violated over extended areas, as it requires a higher energy density.[22c] Second, the alignment boundary may equivalently be located at either a row of singularity points or a homeotropic wall. Once

one of these possibilities is established, every other boundary will present the same situation. Here, two periodicities can be clearly observed: P_x corresponds to the period of the hemitoric FCDs along the x axis and is equal to P_a, whereas P_y represents the distance between adjacent singularity points along the y axis and is equal to 4.7 ± 0.2 μm. This value is slightly smaller than the domain radius, which is attributed to the truncation between vertically neighboring hemitoric FCDs. With the aid of a sensitive tint plate (i.e., full waveplate at $\lambda = 530$ nm), an enhanced anisotropic polarized optical microscopic (POM) texture was obtained (Figure 1l). This image vividly reveals the LC director field and the semicircular profiles of the generated domains. Figure 1m shows an atomic force microscopy (AFM) image of the hemitoric FCD array. The depths of the singularity points are 120–180 nm, which are comparable to those of TFCDs (>100 nm)[15,27] and significantly larger than those of SFCDs (≈20 nm),[22c] validating our assumed hemitoric focal conic model.

We systematically studied the controllability of the unit size of the hemitoric FCDs by varying the alignment period. **Figure 2**a shows various textures of hemitoric FCD superstructures with the same film thickness, at $P_a = 6$ –18 μm. The corresponding AFM images are presented in Figure S4b–h (Supporting Information). Obviously, when 6 μm ≤ P_a ≤ 16 μm (the pink region in Figure 2a), $P_x = P_a$, which means that the domain sizes of the hemitoric FCDs are strictly determined by the alignment period. The relationship between the average values of P_y/P_x and P_a is also graphically presented. All $P_y/P_x \approx 0\%$, consistent with the hemitoric focal conic model. When $P_a > 16$ μm, 18 μm, for example, additional FCDs emerge beside the hemitoric FCDs at single alignment periods. The severe truncation between vertically adjacent hemitoric FCDs causes the P_y/P_x value to decrease. Notably, this value of 18 μm is nearly twice as large as the value of D_a in the freely assembled case (Figure 1f). The emergence of the additional FCDs is an energetic relaxation in response to the anchoring condition. If $P_a \gg D_a$, then textures similar to those seen in Figure 1f will be observed. The color variation among these textures is due to the slight changes in the director field among differently sized domains.
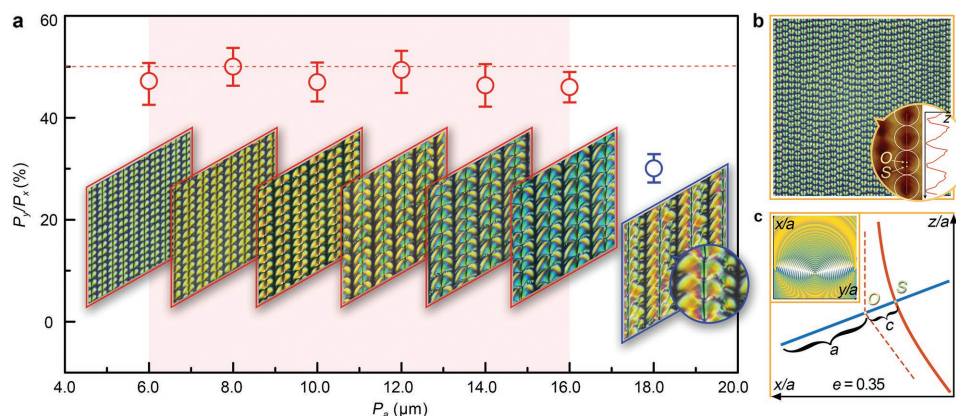

Figure 2. Size tailoring of the hemitoric FCDs by varying the alignment period. a) Dependency of P_y/P_x on P_a, with the corresponding POM textures shown as insets. b) POM texture of the butterfly-like FCDs when $P_a = 4$ μm. Corresponding AFM topographic and cross-section images of the free 8CB/air interface are shown as an inset. The average depth of the holes is ≈60 nm. c) Defect lines and layer configuration of the butterfly-like FCD. a and c are the major-axis and focal distance, respectively, of the ellipse.
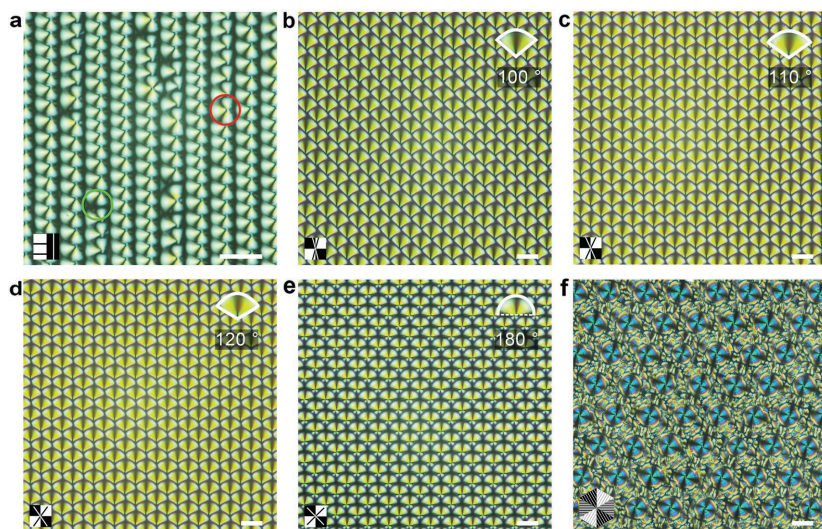
COMMUNICATION

Figure 3. Control of the domain orientation, domain shape, and lattice symmetry. POM textures of a) ±45°-oriented hemitoric FCDs connected by three-quarter toric FCDs (red circle) and defect walls (green circle). P_a = 6 µm. b–e) Square lattices of differently shaped TFCDs generated on multidomain checkerboard photoalignment patterns with adjacent anchoring orientations of ±15°, ±25°, ±35°, and ±45°, respectively. The insets show magnified images of single fragmented TFCDs with the corresponding central angles indicated below them. The checker size is l = 5 µm. f) Hexagonal lattice of artificially induced TFCDs. The anchoring conditions are indicated in the lower-left corner. All scale bars represent 10 µm.

When P_a decreases to 4 µm, a texture of butterfly-like FCDs is observed as the projected points O and S separate (Figure 2b; Figure S4a, Supporting Information). In accordance with the circular domain shape, one asymptote of the hyperbola remains vertical to the substrate, the same as in the SFCD. From the calculated ratio of the eccentric distance $\overline{OS}$ to the average radius R_a of the domains, we set the eccentricity of the ellipse, e (=c/a), to 0.35 and construct the defect lines and layer configuration of the butterfly-like FCD (Figure 2c). An eccentrically radial distribution of the director field is indicated, matching the Maltese cross patterns observed in Figure 2b. Notably, the eccentric direction of the butterfly-like FCD is parallel to the alignment boundaries, and the LC directors in the smaller lobes violate the local anchoring conditions. This is because, for such frequent alternation of the ±45° anchoring directions, the SLC film perceives a mixed anchoring condition similar to that in the case of unidirectional alignment. However, the exact layer configuration should be further confirmed by polarizing fluorescence confocal microscopy[22c] or freeze-fracture transmission electron microscopy.[28]

Since the hierarchical superstructures of unique hemitoric FCDs with exquisitely controlled domain sizes have been created by introducing alternating ±45° alignment regions, the domain orientations with respect to the alignment boundaries are expected to be precisely controlled via similar preprogrammed photoalignment (adjusting the anchoring directions). Here, when the alternating anchoring directions are prescribed to be parallel and perpendicular to the alignment boundaries, ±45°-oriented hemitoric FCDs are produced with equal probability because they are both consistent with the bottom anchoring. They can even coexist, connected by three-quarter toric FCDs or defect walls, as exhibited in **Figure 3**a and

Figure S5 (Supporting Information). On the other hand, the shapes of the fragmented TFCDs can be freely varied. When multidomain checkerboard photoalignment patterns are prepared, square lattices of fragmented TFCDs are formed, with all of the singularity points located at the intersections of alignment boundaries to minimize the free energy (Figure 3b–e). As the anchoring directions change from ±15° to ±45°, the central angle of the generated domains gradually increases from 100° to 180°. By also introducing a predesigned alignment pattern, the central angle can be tuned over a wider range. Moreover, the exact localization of the singularity points enables control of the lattice symmetry. A hexagonal lattice of artificially induced TFCDs was also realized on a multidomain, tridirectionally aligned surface (Figure 3f), which further confirms our proposed hemitoric focal conic model. All the above results indicate that the smectic layer origami can be rationally designed and arbitrarily manipulated. Any desired unit geometry and lattice symmetry can be achieved via preprogramming of the photoalignment pattern and anchoring directions.

Novel optical features can be anticipated from such the hierarchical superstructures of fragmented TFCDs. The sample shown in Figure 3e is utilized as a demonstration. As schematically shown in **Figure 4**a, a square primitive cell with corresponding orthogonal primitive translation vectors a and b ($|a|$ = $|b|$ = $\sqrt{2}$ l) is clearly exhibited, which is directly inherited from the checkerboard alignment pattern. Because of the intentionally introduced alignment periodicity, square diffraction patterns with sharp orders are recorded when a linearly polarized laser beam is normally incident on the sample. When the incident polarization direction is varied, a polarization-dependent diffraction phenomenon is observed (Figure 4b–e). The dependencies of the diffraction efficiency on the rotation angle α of each pair of orders of ±1 are presented in Figure 4f–i. Each curve exhibits repeating peaks and valleys. These phenomena result from a combination of the rotational symmetry breaking of the fragmented hemitoric focal conic unit, the radially gradient LC director field and the arbitrarily designed lattice symmetry. To clearly illustrate the mechanism of the polarization-dependent diffraction phenomenon, selected directional profiles of the effective refractive index (n_{eff}) along four specific rotation angles are presented in Figure 4j–m. When α = 0°, a symmetric triangular n_{eff} profile is extracted (Figure 4j). This is why the orders are symmetrically distributed along the horizontal direction. When α = 45°, 90°, and 135°, asymmetrically serrated n_{eff} profiles are observed (Figure 4k–m), inducing blazed-grating-like diffraction behavior. Therefore, significant contrasts in intensity are induced between the order pairs ($0\overline{1}$) and (01), ($1\overline{1}$) and ($\overline{1}1$), and (10) and ($\overline{1}0$). According to the curves presented in Figure 4f–i, any incident polarization α corresponds to a given energy distribution among the eight orders of ±1. This provides a convenient means of characterizing the

**ADVANCED
SCIENCE NEWS**
www.advancedsciencenews.com
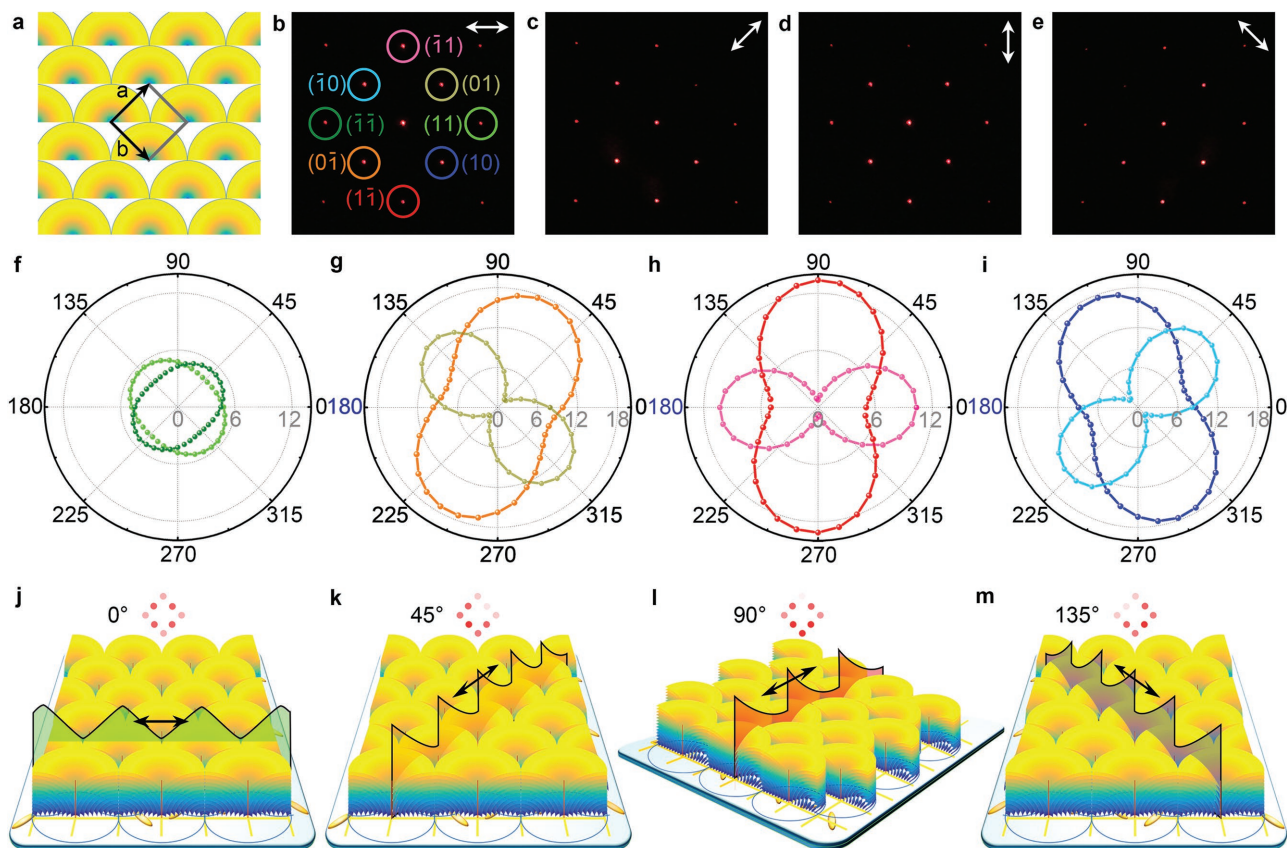
**ADVANCED
MATERIALS**
www.advmat.de

COMMUNICATION

Figure 4. Polarization-dependent diffraction of the hemitoric FCD superstructures. a) Schematic top view of the hemitoric FCD lattice presented in Figure 3e. The gray square and black arrows indicate the square primitive cell and the primitive translation vectors. b–e) Diffraction patterns for incident polarizations of 0°, 45°, 90°, and 135°, respectively. The Miller indices representing the diffraction orders are given in (b). f–i) Curves of diffraction efficiency versus α. Distinctive colors are used that correspond to those of the circles in (b). j–m) n_{eff} profiles along the angles indicated at the top left for the same incident beam polarizations. The corresponding diffraction patterns are schematically exhibited at the top center of each image. The arrows indicate the polarization directions.

polarization by simply measuring the intensity distribution. Such polarization-dependent diffraction also has great potentials in beam steering, polarization imaging, and biomimetic applications.[29]

We propose a new mechanism to manipulate the 3D smectic layer origami via a 2D preprogrammed photoalignment film. It combines the "top-down" photopatterning with the "bottom-up" self-assembling, which pushes the hierarchical architecture of SLCs to an unprecedented level. The principle is rooted in the anisotropy of molecular interactions at the interface between the SLCs and the photoalignment agent, which causes a certain deformation of adjacent smectic layers favored by the prepatterned alignment layer, consequently determining the configuration of the entire family of smectic layers. The adopted digital micromirror device (DMD)-based dynamic photoaligning technique[30] makes the strategy more flexible, high efficient, and suitable for large-area sample preparations. By simply introducing periodic alignment domains with orthogonal anchoring directions, nontrivial hemitoric FCDs are demonstrated for the first time. Such fragmented toric focal conic structure breaks the rotational symmetry, possesses ascertainable orientations, and thus brings two new dimensions: shape and orientation, to the manipulation of hierarchical superstructures. By further

adjusting the anchoring directions and prescribed photopatterns, a full control of the domain geometries (size, shape, and orientation) and lattice symmetry of the hierarchical superstructures is achieved. Thanks to the rotational symmetry breaking, the periodic fragmented TFCDs, which still maintain the radially gradient director field, exhibit a polarization-dependent diffraction phenomenon. In addition, the eccentricity of the ellipse within the FCD is supposed to be tuned in the case of frequent alternation of adjacent anchoring directions, which might add another new dimension to the superstructure manipulation.

In this work, the variations of the shape, size, and orientation of each domain, and the symmetry of FCD lattice all reflect the controlled deformations of smectic layers. It is reasonable to expect for more controllable configuration characteristics and fantastic new hierarchical superstructures. The resultant metasurface-like polarization-dependent diffraction of periodic fragmented TFCDs will definitely enhance the existing technological applications, such as lithographic templates[14a] and microlens arrays,[13] and even can inspire novel designs for optical devices. When the fragmented TFCDs are used as a microlens array, the polarization information will be detected simultaneously with the images, which is very promising in remote sensing and bionic intelligence technology. For these kinds of

samples, the light energy can also be specifically distributed into desired orders by altering the incident polarization, which permits the usage of dedicated beam steering systems. Conversely, the same element can also provide a direct means to characterize the polarization through measuring the intensity distribution. Here, the 3D hierarchical architecture of SLCs is manipulated by preprogramming a 2D photoalignment layer. This concept could be further extended to other soft material systems, colloids, and biological materials for instances. In all, it is an important step forward in expanding the understanding of 3D materials assembly and promoting the construction of remarkable hierarchical superstructures, which suggests additional possibilities for novel functional materials and advanced photonic applications.

Experimental Section

Materials: The SLC material 8CB (4′-Octyl[1,1′-biphenyl]-4-carbonitrile) was purchased from HCCH, China. 8CB exhibits an isotropic–nematic transition at 40.5 °C and a nematic–smectic transition at 33.5 °C. The photoalignment agent sulfonic azo dye SD1 was purchased from Dai-Nippon Ink and Chemicals, Japan. It was dissolved in dimethylformamide at a concentration of 0.3 wt%.

Sample Preparation: Glass slides (1.5 × 2 cm^2) were ultrasonically bathed, UV-ozone cleaned, and then spin coated with SD1. After curing at 100 °C for 10 min, the substrate was placed at the image plane of the DMD-based microlithography system to record the aligning pattern following refs. [30b] and [7a]. Subsequently, one droplet of 8CB was spread on the substrate at 50 °C and spin coated at 3000 rpm for 30 s to achieve a 1.2 μm film. The film thickness was measured at 34 °C (nematic phase) as described in the Supporting Information. All samples were fabricated in this condition to guarantee the formation of FCDs. The spin speed dependent film thickness and textures of thinner films are presented in Figure S6 (Supporting Information).

Characterization: Texture observations were performed using a crossed polarizing microscope (Nikon 50i, Japan). Surface morphology characterizations were performed using a commercial atomic force microscope (Dimension Icon, Bruker, USA). All substrates were imaged in tapping mode in air, using standard RTESP cantilevers with a nominal spring constant of 40 N m^{-1}. The typical scanning rates were in the range of 0.5–1 Hz per line. For the diffraction measurements, a linearly polarized He–Ne laser at λ = 632.8 nm was normally incident on the sample. Diffraction patterns were captured by a digital camera (EOS M Canon, Japan) at different relative angles.

Supporting Information

Supporting Information is available from the Wiley Online Library or from the author.

Acknowledgements

[1] G. Cao, *Nanostructures and Nanomaterials: Synthesis, Properties and Applications*, Imperial College Press, New York **2004**.

[2] a) G. M. Whitesides, B. Grzybowski, *Science* **2002**, *295*, 2418; b) J. V. Barth, G. Costantini, K. Kern, *Nature* **2005**, *437*, 671.

[3] a) M. Thomé, L. Nicole, S. Berthier, *Mater. Today* **2014**, *1*, 221; b) S. Yoshioka, S. Kinoshita, *Forma* **2002**, *17*, 169.

[4] Y. T. Cheng, D. E. Rodak, C. A. Wong, C. A. Hayden, *Nanotechnol.* **2006**, *17*, 1359.

[5] X. Gao, L. Jiang, *Nature* **2004**, *432*, 36.

[6] a) A. Honglawan, S. Yang, *Nanoscience with Liquid Crystals: From Self-Organized Nanostructures to Applications*, Springer International Publishing, Cham, Switzerland **2014**, Ch. 2; b) H. K. Bisoyi, Q. Li, *Acc. Chem. Res.* **2014**, *47*, 3184; c) H. K. Bisoyi, Q. Li, *Chem. Rev.* **2016**, *116*, 15089.

[7] a) L. L. Ma, S. S. Li, W. S. Li, W. Ji, B. Luo, Z. G. Zheng, Z. P. Cai, V. Chigrinov, Y. Q. Lu, W. Hu, L. J. Chen, *Adv. Opt. Mater.* **2015**, *3*, 1691; b) H. C. Jau, Y. Li, C. C. Li, C. W. Chen, C. T. Wang, H. K. Bisoyi, T. H. Lin, T. J. Bunning, Q. Li, *Adv. Opt. Mater.* **2015**, *3*, 166; c) Z. G. Zheng, Y. Li, H. K. Bisoyi, L. Wang, T. J. Bunning, Q. Li, *Nature* **2016**, *531*, 352; d) J. Kobashi, H. Yoshida, M. Ozaki, *Nat. Photonics* **2016**, *10*, 389.

[8] a) H. Kikuchi, M. Yokota, Y. Hisakado, H. Yang, T. Kajiyama, *Nat. Mater.* **2002**, *1*, 64; b) H. J. Coles, M. N. Pivnenko, *Nature* **2005**, *436*, 997; c) M. Ravnik, G. P. Alexander, J. M. Yeomans, S. Žumer, *Proc. Natl. Acad. Sci. USA* **2011**, *108*, 5188.

[9] a) T. H. Lin, Y. J. Chen, C.-H. Wu, A. Y. G. Fuh, J. H. Liu, P. C. Yang, *Appl. Phys. Lett.* **2005**, *86*, 161120; b) S. Yokoyama, S. Mashiko, H. Kikuchi, K. Uchida, T. Nagamura, *Adv. Mater.* **2006**, *18*, 48.

[10] a) D. W. Berreman, W. R. Heffner, *Appl. Phys. Lett.* **1981**, *52*, 3032; b) Z. Ge, L. Rao, S. Gauza, S. T. Wu, *J. Disp. Technol.* **2009**, *5*, 250.

[11] a) G. Friedel, *Ann. Phys* **1922**, *18*, 273; b) Y. Bouligand, *J. Phys.* **1972**, *33*, 525.

[12] a) Y. H. Kim, D. K. Yoon, H. S. Jeong, J. H. Kim, E. K. Yoon, H. T. Jung, *Adv. Funct. Mater.* **2009**, *19*, 3008; b) D. S. Kim, Y. J. Cha, H. Kim, M. H. Kim, Y. H. Kim, D. K. Yoon, *RSC Adv.* **2014**, *4*, 26946.

[13] Y. H. Kim, H. S. Jeong, J. H. Kim, E. K. Yoon, D. K. Yoon, H. T. Jung, *J. Mater. Chem.* **2010**, *20*, 6557.

[14] a) Y. H. Kim, D. K. Yoon, H. S. Jeong, H. T. Jung, *Soft Matter* **2010**, *6*, 1426; b) D. S. Kim, A. Honglawan, K. Kim, M. H. Kim, S. Jeong, S. Yang, D. K. Yoon, *J. Mater. Chem. C* **2015**, *3*, 4598; c) H. W. Yoo, Y. H. Kim, J. M. Ok, H. S. Jeong, J. H. Kim, B. S. Son, H. T. Jung, *J. Mater. Chem. C* **2013**, *1*, 1434.

[15] Y. H. Kim, J. O. Lee, H. S. Jeong, J. H. Kim, E. K. Yoon, D. K. Yoon, J. B. Yoon, H. T. Jung, *Adv. Mater.* **2010**, *22*, 2416.

[16] W. Guo, C. Bahr, *Phys. Rev. E* **2009**, *79*, 011707.

[17] D. S. Kim, Y. J. Cha, M. H. Kim, O. D. Lavrentovich, D. K. Yoon, *Nat. Commun.* **2016**, *7*, 10236.

[18] J. M. Ok, Y. H. Kim, H. S. Jeong, H. W. Yoo, J. H. Kim, M. Srinivasarao, H. T. Jung, *Soft Matter* **2013**, *9*, 10135.

[19] a) W. Guo, S. Herminghaus, C. Bahr, *Langmuir* **2008**, *24*, 8174; b) J. P. Bramble, S. D. Evans, J. R. Henderson, T. J. Atherton, N. J. Smith, *Liq. Cryst.* **2007**, *34*, 1137.

[20] a) D. K. Yoon, M. C. Choi, Y. H. Kim, M. W. Kim, O. D. Lavrentovich, H. T. Jung, *Nat. Mater.* **2007**, *6*, 866; b) S. Shojaei-Zadeh, S. L. Anna, *Langmuir* **2006**, *22*, 9986; c) Y. H. Kim, D. K. Yoon, M. C. Choi, H. S. Jeong, M. W. Kim, O. D. Lavrentovich, H. T. Jung, *Langmuir* **2009**, *25*, 1685; d) J. H. Kim, Y. H. Kim, H. S. Jeong, E. K. Youn, H. T. Jung, *J. Mater. Chem.* **2011**, *21*, 18381.

[21] A. Honglawan, D. A. Beller, M. Cavallaro, R. D. Kamien, K. J. Stebe, S. Yang, *Adv. Mater.* **2011**, *23*, 5519.

[22] a) J. P. Michel, E. Lacaze, M. Goldmann, M. Gailhanou, M. de Boissieu, M. Alba, *Phys. Rev. Lett.* **2006**, *96*, 027803; b) T. Ohzono, Y. Takenaka, J. I. Fukuda, *Soft Matter* **2012**, *8*, 6438; c) B. Zappone, C. Meyer, L. Bruno, E. Lacaze, *Soft Matter* **2012**, *8*,

ADVANCED
SCIENCE NEWS
www.advancedsciencenews.com

ADVANCED
MATERIALS
www.advmat.de

COMMUNICATION

4318; d) A. Honglawan, D. A. Beller, M. Cavallaro, R. D. Kamien, K. J. Stebe, S. Yang, *Proc. Natl. Acad. Sci. USA* **2013**, *110*, 34.

[23] a) K. Ichimura, *Chem. Rev.* **2000**, *100*, 1847; b) M. Schadt, H. Seiberle, A. Schuster, *Nature* **1996**, *381*, 212; c) V. G. Chigrinov, V. M. Kozenkov, H. S. Kwok, *Photoalignment of Liquid Crystalline Materials: Physics and Applications*, John Wiley & Sons, West Sussex, UK **2008**; d) M. Schadt, H. Seiberle, A. Schuster, S. M. Kelly, *Jpn. J. Appl. Phys.* **1995**, *34*, L764.

[24] M. Kleman, O. D. Lavrentovich, *Liq. Cryst.* **2009**, *36*, 1085.

[25] H. Akiyama, T. Kawara, H. Takada, H. Takatsu, V. Chigrinov, E. Prudnikova, V. Kozenkov, H. Kwok, *Liq. Cryst.* **2002**, *29*, 1321.

[26] Y. H. Kim, D. K. Yoon, H. S. Jeong, O. D. Lavrentovich, H. T. Jung, *Adv. Funct. Mater.* **2011**, *21*, 610.

[27] V. Designolle, S. Herminghaus, T. Pfohl, C. Bahr, *Langmuir* **2006**, *22*, 363.

[28] D. K. Yoon, Y. H. Kim, D. S. Kim, S. D. Oh, I. I. Smalyukh, N. A. Clark, H. T. Jung, *Proc. Natl. Acad. Sci. USA* **2013**, *110*, 19263.

[29] L. Wang, Q. Li, *Adv. Funct. Mater.* **2016**, *26*, 10.

[30] a) H. Wu, W. Hu, H. C. Hu, X. W. Lin, G. Zhu, J. W. Choi, V. G. Chigrinov, Y. Q. Lu, *Opt. Express* **2012**, *20*, 16684; b) B. Y. Wei, W. Hu, Y. Ming, F. Xu, S. Rubin, J. G. Wang, V. Chigrinov, Y. Q. Lu, *Adv. Mater.* **2014**, *26*, 1590.